*Stochastic Modelling and Computational Sciences*

# SEISMIC ANALYSIS OF OFFSHORE WIND TURBINES MONOPILES WITH DIFFERENT CONFIGURATIONS

**Tarek N. Salem[1] and Mohamed M. Hussein[2]**
[1]Professor and [2]Teaching Assistant, Department of Structural Engineering, Faculty of Engineering, Zagazig University, Zagazig, Egypt

## ABSTRACT
*Earthquake impacts affect offshore wind farms in seismically active places. Seismic analysis of a monopile offshore wind turbine in various configurations is done in this paper. A finite element model for a monopile of offshore wind turbine is conducted using the Plaxis-3D software. More research investigations are needed to have a better knowledge of this issue due to the rapid spread of wind energy and the increasing number of wind turbines built in seismic activity locations. The main research objective is exploring the effect of different monopile configurations on the seismic response of its foundations. The effects of turbines under static and seismic loads have been considered in this study. Time history analysis is carried out to study the behavior of monopiles under three different earthquake records including; Northridge 1994, Chi-Chi 1999, and Friuli 1976. It is noticed that the maximum displacement took place at the pile top. Results show that a standard monopile with diameter of 4.00 m has almost the same behavior as a winged monopile of a diameter of 2.80 m with additional wings having lower material cost.*

*Keywords: Offshore, Wind Turbines, Earthquake, Seismic Response, Plaxis 3D.*

## 1. INTRODUCTION
Offshore wind energy is desirable because of its enormous reserves, lack of land occupancy, and little impact on humans [1]. It is well understood that earthquake movements from coastal land to offshore waters can significant harm to the safety of offshore wind generators in seismically active places [2, 3]. Because earthquakes are unexpected, when an earthquake happens, offshore wind turbines may be operating under varied operational circumstances [4, 5]. Seismic forces produce various nonlinear dynamic responses for offshore wind turbines, which might reach structural limit states and result in collapse of both the power generating system and the supporting monopile. Thus, studies should be carried out to better understand the responses of offshore wind turbines to seismic loads for monopiles of various shapes and configurations.

The majority of research concentrated on onshore wind turbines, which have shorter cantilever lengths than offshore ones. Furthermore, onshore wind turbines are supported by relatively firm foundations and are not exposed to water waves. Lavassas et al. [6] studied the reactions of a 1 MW wind turbine on a concrete circular foundation in rocky soil under combined wind and earthquake loadings and discovered that seismic loads were important when the wind turbine tower was built in seismically dangerous locations and on medium or soft soil grounds. Prowell [7] stated that as wind turbine size increased consideration of dynamics and operating state become increasingly critical. Prowell's research also revealed the importance of soil-structure interaction, particularly for massive wind turbines.

Sapountzakis et al. [8] investigated the dynamic reactions of a 5 MW wind turbine on either a surface or monopile foundation system, and discovered that modeling soil-structure interaction was critical in the understanding of wind turbine seismic response. Ma [9] conducted research on the dynamic behavior of wind turbines exposed to both vertical and horizontal earthquake components. The analysis found that, in seismically active areas, it was crucial to take earthquake loads into account for moment demand and vertical load in the tower of the 1.65 and 3.0 MW reference turbines.

Kourkoulis et al. [10] non-linear three-dimensional finite element analysis is used to examine the seismic reactions of suction caisson foundations for offshore wind turbines, although static wind and wave forces are used in place of time history loads. Anastasopoulos and Theofilou [11] the performance of a hybrid foundation for

 

offshore wind turbines under environmental and seismic forces is investigated. The addition of the footing to the monopile resulted in a significant increase in moment capacity, according to the results.

On the other hand, more current study is still being done on the seismic safety of offshore wind farms. To examine the safety of the wind turbine constructions and to better understand the seismic responses of offshore wind turbines for various monopile layouts. The purpose of this study is to investigate the seismic response of offshore wind turbines having different foundation configurations.

The studied case is a Vestas 2.0 MW monopile offshore wind turbine using Plaxis software; the dynamic responses of the wind turbine assembly are studied using the finite element method.

## 2. FINITE ELEMENT ANALYSIS USING PLAXIS 3D

Nonlinear constitutive models are needed for modeling the soil and pile materials for seismic foundation-soil system analyses. Therefore, Plaxis 3D program is used to achieve this target. It is three-dimensional finite element software designed to simulate geotechnical engineering issues. A variety of predefined material models are available for modeling soil behavior, deformation analysis, stability, groundwater flow, and earthquakes in geotechnical engineering [16][17].

### 2.1 Interface Element

To represent contact between soil and structural components, interfaces must be defined to provide a lower strength between a structure surface and the soil. Without interface components, no slippage or gapping is permitted, which is a non-physical assumption for the interaction of structure and soil in most circumstances thus the elastic-plastic interface material model employed in this study.

### 2.2 Boundary Conditions

#### 2.2.1 Standard Boundary Conditions

Plaxis 3D adds standard fixities to the model's boundaries, as seen in Figure 1. Vertical boundaries are free in the z direction and the lateral direction parallel to the boundary plane by default, but fixed in the normal direction. The top surface is free in all directions by default, but the bottom surface is totally fixed [18][19].

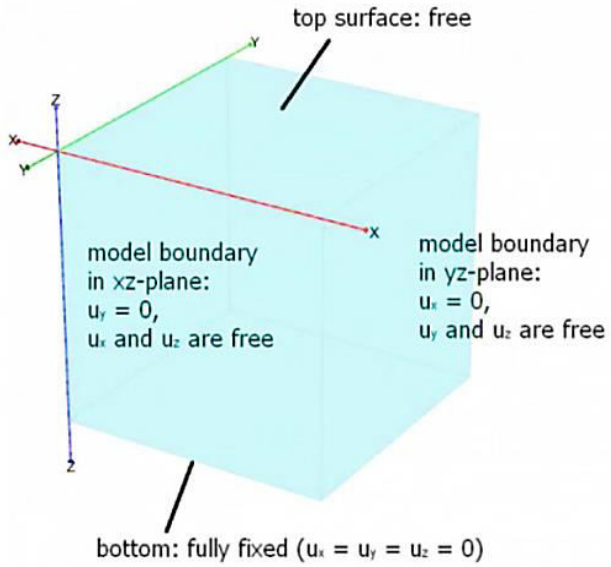


**Figure 1:** Default Boundary Conditions in Plaxis 3D.

### 2.3 Verification of the Numerical Model

This verification depends on the soil characteristics at Dunkirk location that is employed during the PISA project for laterally loaded monopile tests in dense sand (McAdam et al., 2020). All Plaxis 3D calibration calculations, termed herein, are carried out with Hardening Soil Model (Benz, 2007) as shown in Table 1. For the soil profile $E_{50,ref}$ = 60 MPa , $E_{oed,ref}$ = 60 MPa and $P_{ref}$ = 100 kPa.

Results obtained during monopile testing are used to verify the numerical model which is performed using the finite element software Plaxis with different properties, as shown in Table 2 and Figure 2. The monopile itself is a steel tube and modeled as a linear elastic material because of the large differences between the soil and steel stiffness. Summary of the input parameters are presented in Table 3 [20][21].

**Table 1:** Hardening Soil Model with Small Strain Stiffness Properties (Minga, 2019)**.**

| Layer | Depth | $RD^{real}$ (%) | Ko | $\gamma_{sat}$ (kN/m$^3$) | $c'_{ref}$ (kPa) | $\phi'$ (°) | $\psi$ (°) | $\phi'_{int}$ (°) | $G_{0,ref}$ (MPa) | $E_{ur,ref}$ (MPa) | $\gamma_{0.70}$ | $R_f$ |
|---|---|---|---|---|---|---|---|---|---|---|---|---|
| **1** | 0-3 | 100 | 0.40 | 17.10 | 5 | 44 | 15 | 29 | 196,852 | 460,633 | 0.0001 | 0.875 |
| **2** | 3-5.40 | 75 | 0.40 | 17.10 | 10 | 40 | 10 | 29 | 169,675 | 397,040 | 0.000125 | 0.906 |
| **3** | 5.40-10 | 75 | 0.40 | 19.90 | 0.10 | 40 | 10 | 29 | 165,878 | 388,155 | 0.000125 | 0.906 |
| **4** | 10-20 | 75 | 0.40 | 19.90 | 0.10 | 40 | 10 | 29 | 156,998 | 367,376 | 0.000125 | 0.906 |

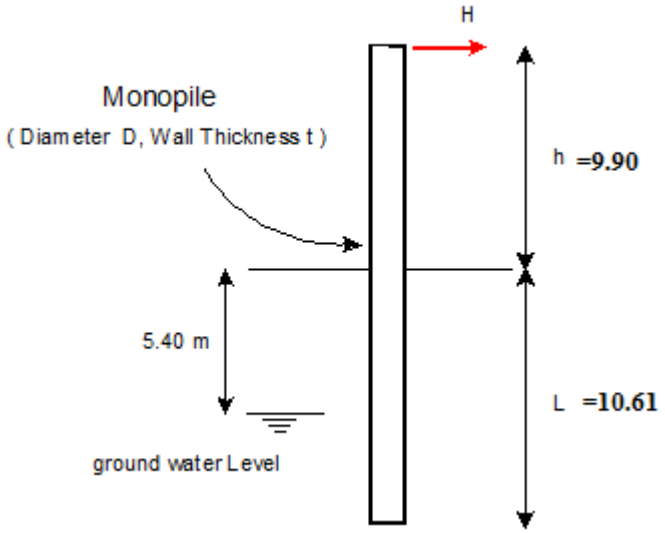


**Figure 2**: Monopile Dimensions and Properties.

**Table 2:** Pile Model Parameters.

| Parameter | MonoPile, Elastic (Isotropic Model) |
|---|---|
| Modulus of Elasticity, E (GPa) | 200.0 |
| Unit Weight, γ (kN/m$^3$) | 78.50 |
| Poisson's ratio, ν | 0.30 |
| Diameter , m | 2.00 |
| Thickness , cm | 3.80 |

Figure 3 illustrates the 3D plaxis analysis response that is in good agreement with the field data. Field test data and associated finite element comparisons are of similar magnitude. The field load is equal to 4,100 kN and the numerical load for full model is 4,096 kN at ground displacement of (10% D) = 0.20 m. Therefore, the numerical results are consistent with the experimental ones.

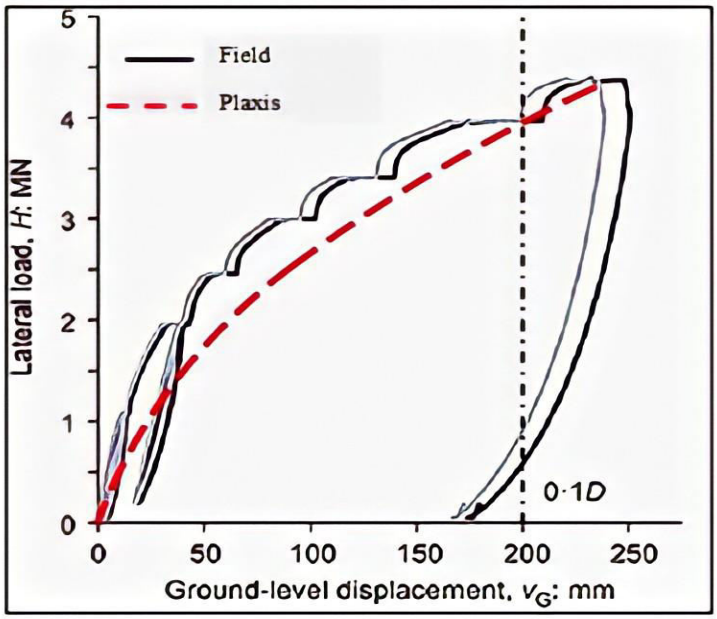


**Figure 3:** Comparisons between Field and 3D Plaxis Model Outcomes for Monopile Tested at Dunkirk; Horizontal Load, H, vs. Ground Displacement, $V_G$, Response.

### 2.4 Dynamic Model Boundaries

The boundaries for dynamic calculations should, in general, be much wider apart than those for static calculations, since otherwise, stress waves will be reflected back into the soil domain, causing distortions in the calculated results. Locating the limits far away, on the other hand, necessitates many more parts and hence a lot of extra memory and computing time. Plaxis employs the following dynamic model boundaries to combat reflections and avoid false waves [22][23].

### Viscous Boundaries 2.4.1

The concept of viscous boundaries dates back to the late 1960s, when Lysmer and Kuhlmeyer (1969) applied the principle of absorbing incoming waves. This absorbing boundary can compensate for reflected stresses induced by dynamic input. The usefulness of viscous boundaries is restricted to dynamic sources that must be contained within the mesh. Furthermore, it is incompatible with structural components (Galavi et al., 2013 and Plaxis Manual) [12].

Instead of applying fixities in a certain direction, viscous boundaries are employed with a damper. The damper guarantees that an increase in boundary stress is absorbed without rebounding. The border then begins to move. The normal and shear stress components absorbed by an x-direction damper are shown in equations (1) and (2).

$$\sigma_n = -C_1 \rho V_p \dot{u}_x \quad (1)$$

$$\tau = -C_2 \rho V_s \dot{u}_y \quad (2)$$

Where ρ is density of material, $V_p$, $V_s$ are the pressure and shear wave velocities respectively, $\dot{u}x$ and $\dot{u}y$ are the normal and shear particle velocities derived by time integration and C1, C2 are relaxation factors to develop the influence of absorption. $C_1 = C_2 = 1$ and $C_1 = 1$, $C_2 = 0.25$ for normal and shear waves respectively [13].

### 2.4.2 Free-Field and Compliant Base Boundaries

The free field boundary condition is an additional column next to the primary model's vertical boundary that simulates far field with minimal reflection. The free field boundary takes into account reflected wave absorption from internal anomalies (Galavi et al., 2013 and Plaxis Manual) [12]. The free field border can only be used on the model's lateral sides. Plaxis provides a compliant base at the model's base, which is analogous to the free field.

Compliant base boundaries work on the same idea of absorbing outgoing waves into the infinite space under the model base, but with the added capability of transferring prescribed dynamic loads up into the model.

The free field boundary conditions are only available for the lateral boundaries, i.e. x_min/x_max, and y_min/y_max (3D). The free field boundaries are composed of a load history and a viscous boundary. The load history represents the load resulting from free field motion at this level. The combination of a load history and a viscous boundary allows an earthquake motion to be input while still absorbing incoming waves. In general, this approach is recommended for earthquake analysis. In a free-field boundary, the area is reduced to the domain of interest, and free field motion is applied to the boundaries using free-field elements. As shown in Figure 4, a free-field element is a one-dimensional element in a two-dimensional problem that is related to the main grid by viscous dashpots. The same mechanical characteristics as the nearby soil element in the main domain are employed to determine wave propagation in inner elements. To eliminate wave reflection from interior structures (or sources within the domain), the primary domain boundary is encircled by viscous boundaries, as shown in Figures 4 and 5 [13].

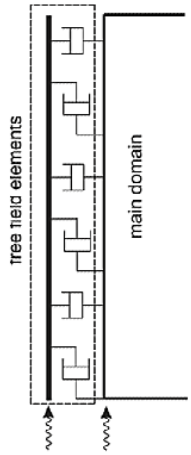


**Figure 4:** Free Field Elements.

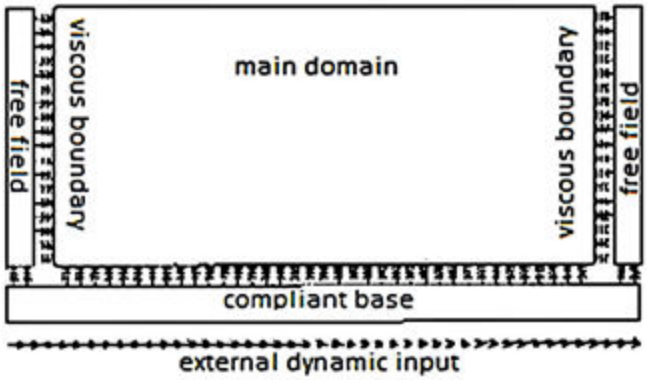


**Figure 5:** Free Field Boundary Condition with Compliant Base (No Wave Reflection at Base).

The free field motion is transmuted from elements at free field domain to the core area by application of equivalent forces according to equations (3) and (4). These equations show how viscous boundaries affect the model boundaries to absorb the reflected internal structures waves [13]:

$$\sigma n = - C_1 \rho V_p (\dot{u}_x^m - \dot{u}_x^{ff}) \quad (3)$$

$$\tau = - C_2 \rho V_s (\dot{u}_y^m - \dot{u}_y^{ff}) \quad (4)$$

Where $\dot{u}^{m}$, $\dot{u}^{ff}$ are the particle velocities in the main grid and in the free-field element respectively and $C_1$, $C_2 = 1$.

As shown in Fig. 4 and Fig. 5, free-field elements can be attached to the lateral boundaries of the main domain. If the bottom cluster is taken into consideration, dynamic excitation input and absorption can be done at the same boundary (at the bottom level of the model) [14]. The equivalent stresses in a compliant base are given by equations (5) and (6).

$$\sigma_n = - C_1 \rho V_p (\dot{u}_x^d - \dot{u}_x^u) \quad (5)$$

$$\tau = - C_2 \rho V_s (\dot{u}_y^d - \dot{u}_y^u) \quad (6)$$

Where $\dot{u}u$ and $\dot{u}d$ are the upward and downward particle velocities, which can be considered as displacement in the element and the main domain, respectively. If the tangential relaxation coefficient C2 is equal to one, the compliant base operates properly. Because half of the input is absorbed by the viscous dashpots and half is transported into the main domain, the reaction of the dashpots is increased by a factor of two. This is the distinction between compliant and free field boundary conditions.

For seismic analysis of prototypes, the compliant base and free-field boundaries are commonly preferred. However, in terms of model testing, the other two boundaries can imitate genuine behavior. Table 3 in this paper shows the boundary conditions for the seismic analysis [24][25].

**Table 3:** Boundary Conditions in Seismic Analysis.

| | Boundary Condition |
|---|---|
| Top Surface | None |
| Lateral Surfaces | Free Field |
| Bottom Surface | Compliant Base |

### 3. Earthquake Records

The Northridge earthquake record (1994) is utilized as input motion that acted at the SSI model's bottom boundary. The Northridge accelogram is utilized to give input for the seismic response of the monopile for 39.98 seconds as ground acceleration time history Figure 6. The water particle kinematics is considered to be zero in the seismic analysis alone. Northridge record has been used to apply seismic inputs.

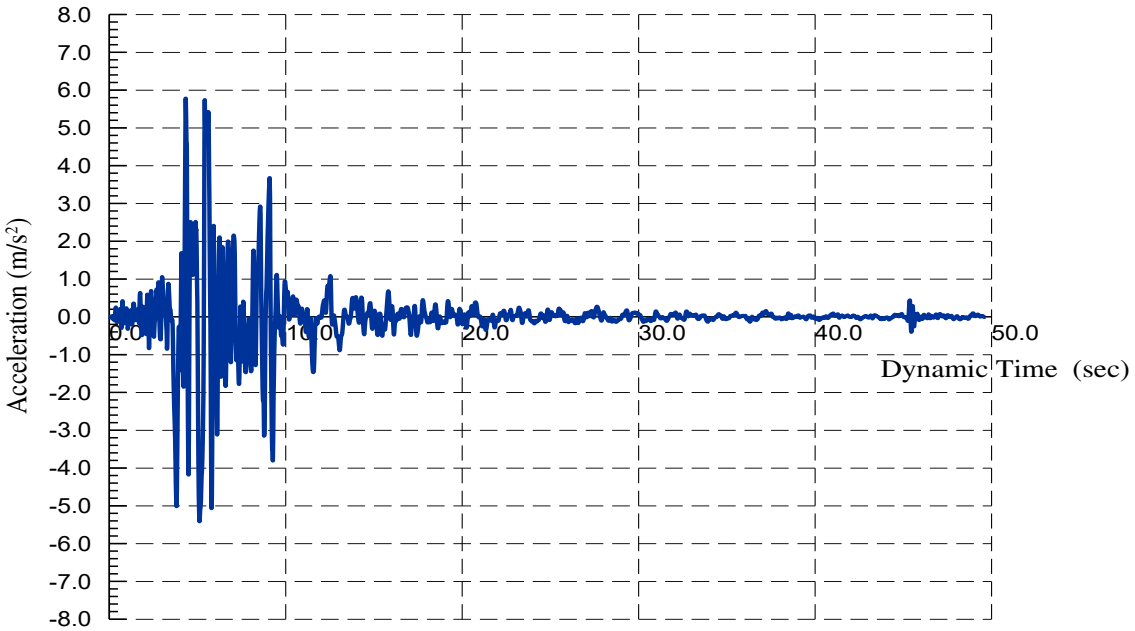


**Figure 6:** Northridge Earthquake Acceleration-Time History.

In this study, the detailed soil investigation data including unit weight and soil strength parameters are used for analysis of the ground response using Plaxis 3D, and the soil classes investigated are illustrated in Table 4. The soil parameters are obtained from soil investigation of Zafrana wind farm, as presented in Saudi, 2020.

**Table 4:** Soil Profile Including Average Values of the Strength and Stiffness Parameters in Zafarana, (Saudi, 2020).

| Layer | Depth | C (kPa) | ϕ (°) | ψ (°) | E (MPa) | □ |
|---|---|---|---|---|---|---|
| **1** | 0-10 | 0 | 37 | 7 | 40.00 | 0.35 |
| **2** | 10.00-18.80 | 100 | 0 | 0 | 30.00 | 0.45 |
| **3** | 18.80-30.0 | 250 | 0 | 0 | 90.00 | 0.23 |

The monopile is exposed to a static maximum horizontal load H = 4.6 MN operating at a height of h = 20.65 m above seabed level and a water level of 13.50 m above seabed level.

The calculations are divided into four separate steps, which are listed below:

1- Initial phase. A default phase in PLAXIS 3D to set and compute the initial soil stresses using a specific built-in Plaxis function that takes into consideration the soil's loading history. The lateral earth pressure coefficient at rest, Ko, is employed in this case.

2- Phase 2 (static loads). Structure installation: Enable the geometry of the foundation and the entire structure's self-weight, then execute static calculations before applying the additional loads in the following step. In this step, the calculation type is set to Plastic calculation.

3- Phase 3 (earthquake). The dynamic analysis simulates earthquake excitation. Because the free field components and the compliant base are employed at the boundaries, an interface is required to activate the boundary conditions.

4- Phase 4 (final static phase) is carried out, which both monitors the dissipation of the excess pore water pressure created during the dynamic analysis and computes the final lateral pile head displacement.

5- Except for the dynamic calculation, where the number of maximum steps and sub-steps must meet the following criterion, the default calculation parameters are applicable in all stages:

$\Delta t = \delta_t (m \cdot n)$

where

$\Delta t$: Duration of dynamic loading (dynamic time interval).

$\delta_t$: Time step, this is equal to the time step of the signal used as input load.

m: Number of steps.

n: Number of sub-steps.

**4. Dynamic Responses of the Monopile**

Figure (7) presents the displacement-time history of selected points at mud level, pile top and pile tip and the signature of north ridge earthquake. Results show that the maximum displacement of all the studied points occurred at the time of the maximum earthquake amplitude. It is apparent that the deformation increased with the height above the seabed and that the maximum displacement occurred at the top in the lateral direction and the maximum displacement gradually increased with increasing the height of the monopile structure above the seabed.

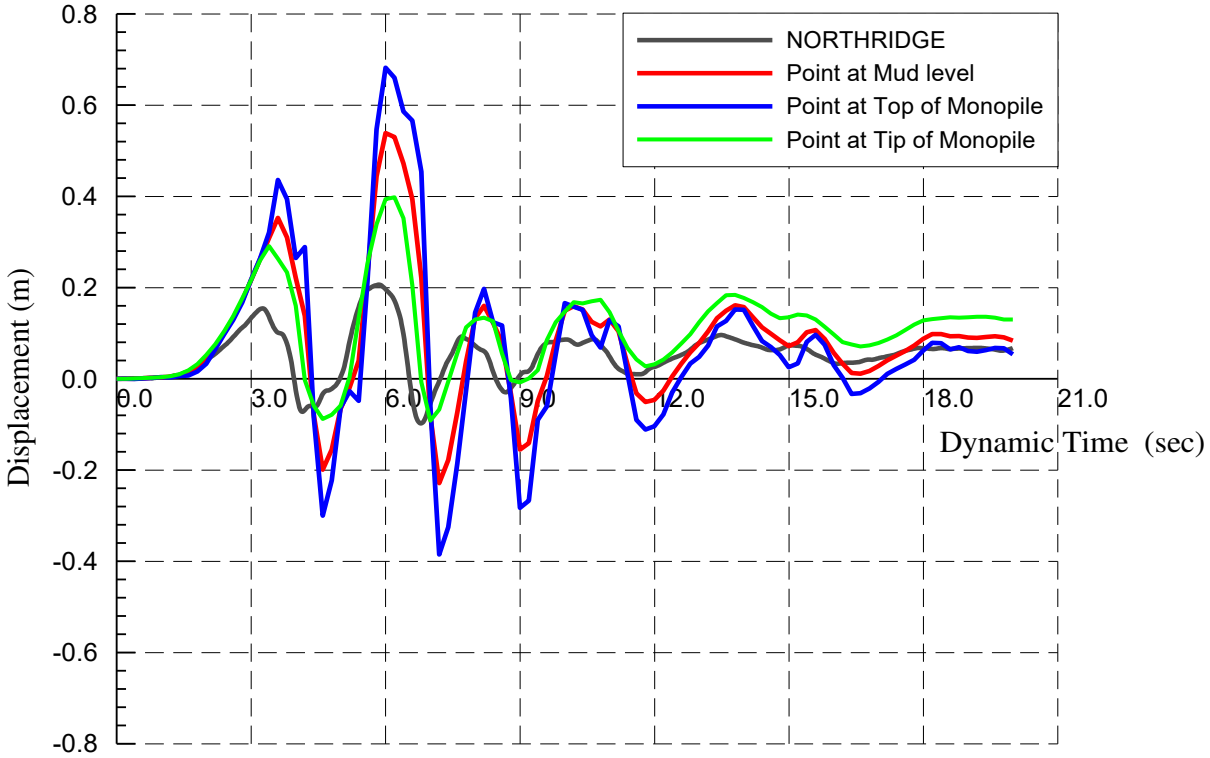


**Figure 7:** Displacement-Time History at Different Points along the Monopile for Northridge Earthquake Record Case.

Figure (8) displays the distribution of the excess pore water pressure in the entire soil domain after 6 seconds (at the maximum earthquake displacement), which shows that the maximum positive excess pore water pressure occurred at the pile tip. Negative pore water pressures can also be observed just below the pile tip.

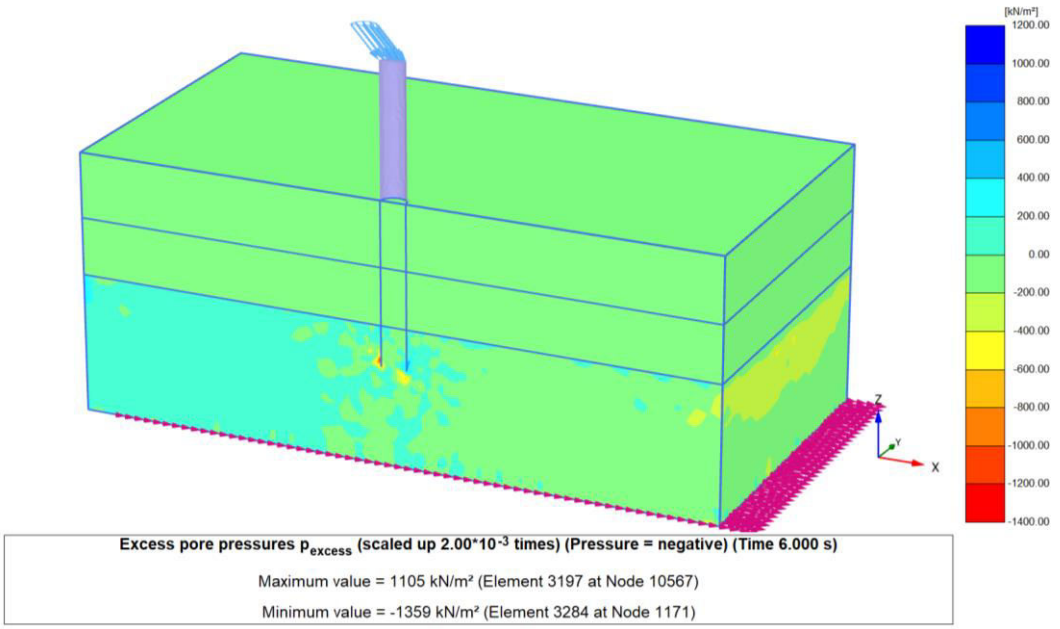


**Figure 8:** Excess Pore Pressure Shading (Time 6 sec).

Figure (9) presents the relation between the time history distribution of the excess pore water pressure at the pile tip. Results show that the maximum excess negative pore water pressure = -230 kPa and the positive value = 100 kPa occurred at peak time of the earthquake displacement. Under seismic conditions, this is mainly alternating positive and negative pore water pressure accumulation. It should be noted that for loose saturated sands, if the accumulation of positive excess pore water pressure continues for relatively longer period of time, liquefaction will take place under the pile tip which would be hazardous to the monopile stability.

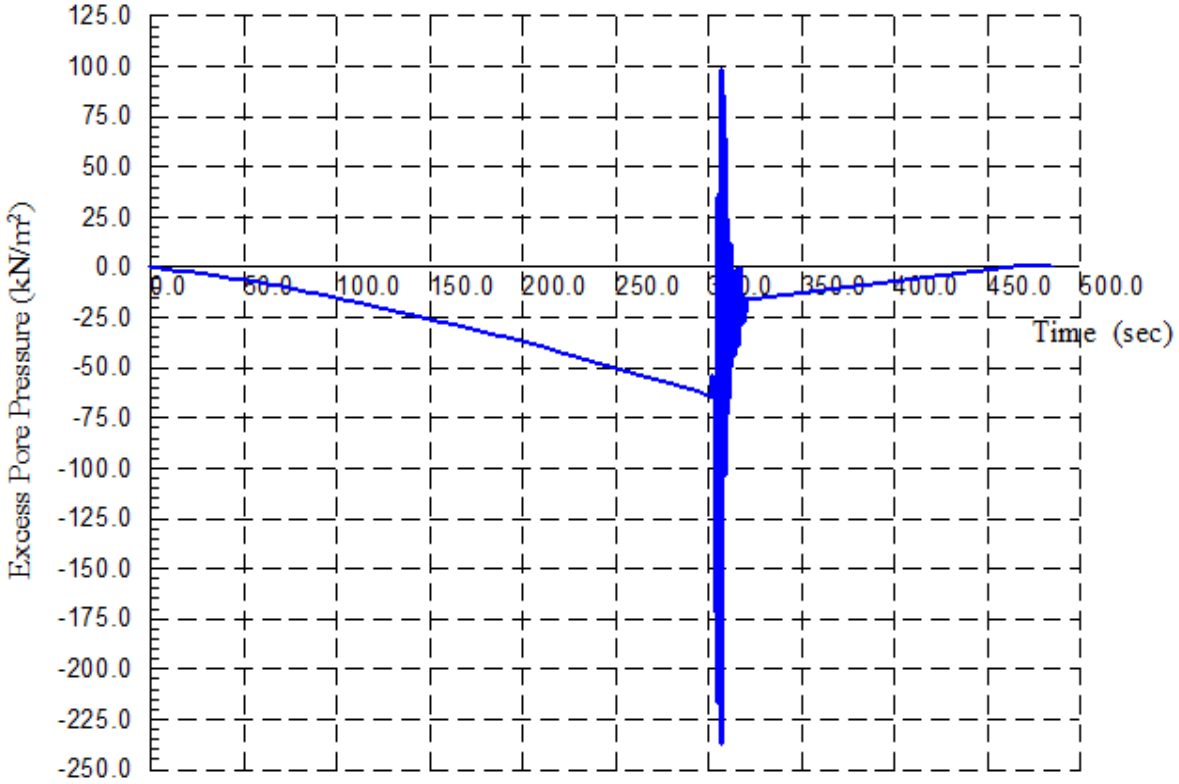


**Figure 9:** Excess Pore Pressure Time Curve at Monopile Tip.

### 4.1. Top Winged Monopile

Grabe et al. (2005) suggested that expanding the cross-sectional area of the piles at the mud level will increase the lateral load capacity of monopile foundations. The installation of steel wings (or fins) to the pile body near the mud line is one technique for increasing the pile lateral resisting area, as presented in Figure (10). Four steel wings are attached to the monopile body, with wing length, $h_w$ = 5.60 m, breadth, $b_w$ = 2.80 m, pile diameter = 2.80 m, and wall thickness = 5.0 cm respectively at each side of the pile. The standard cylindrical equivalent monopile of diameter = 4.00 m, and having the same wall thickness = 5.0 cm.

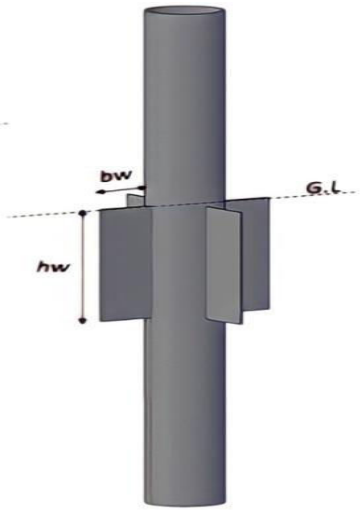


**Figure (10):** Top Winged Monopile, with Wings Located at the Mud Line.

### 4.2. Effect of Earthquake Record

Three different seismic records are used in the dynamic analysis, namely; Northridge, Chi-Chi, and Friuli. The monopile lateral behavior is studied using the three different seismic records. Northridge record is shown in Figure 6, Chi-Chi earthquake record is shown in Figure 11, and the Friuli earthquake record is presented in Figure 12.

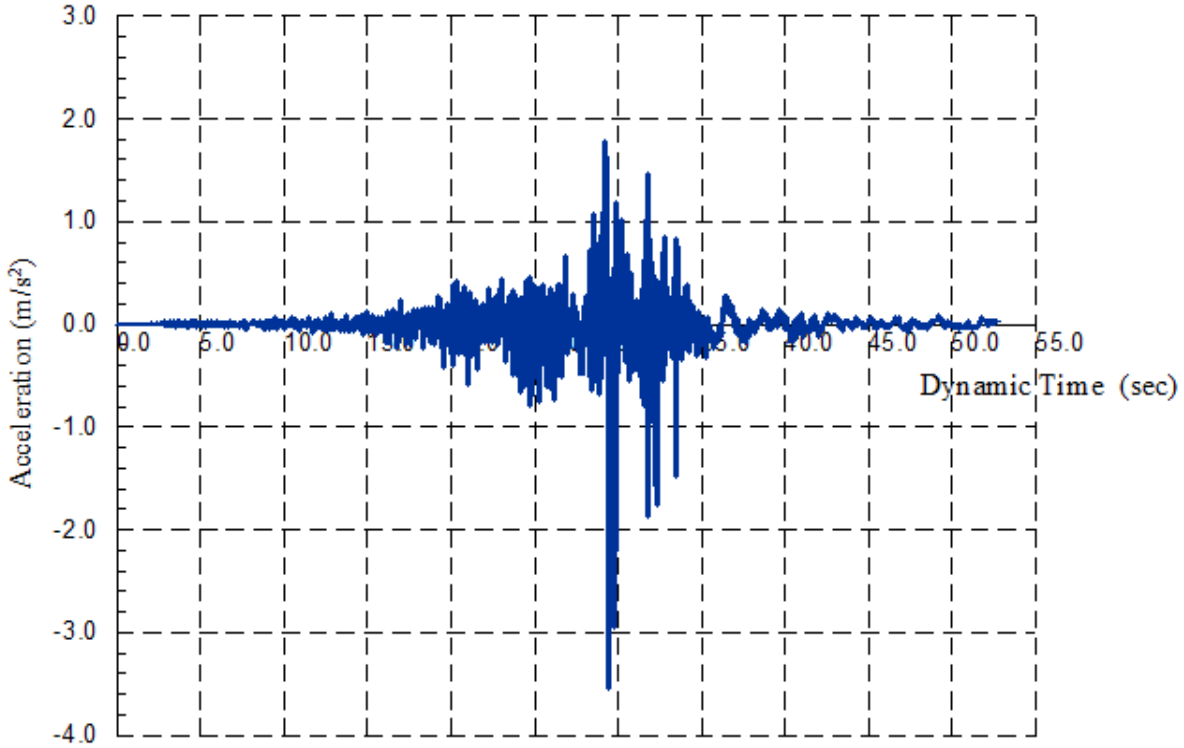


**Figure 11:** Chi-Chi Earthquake Record.

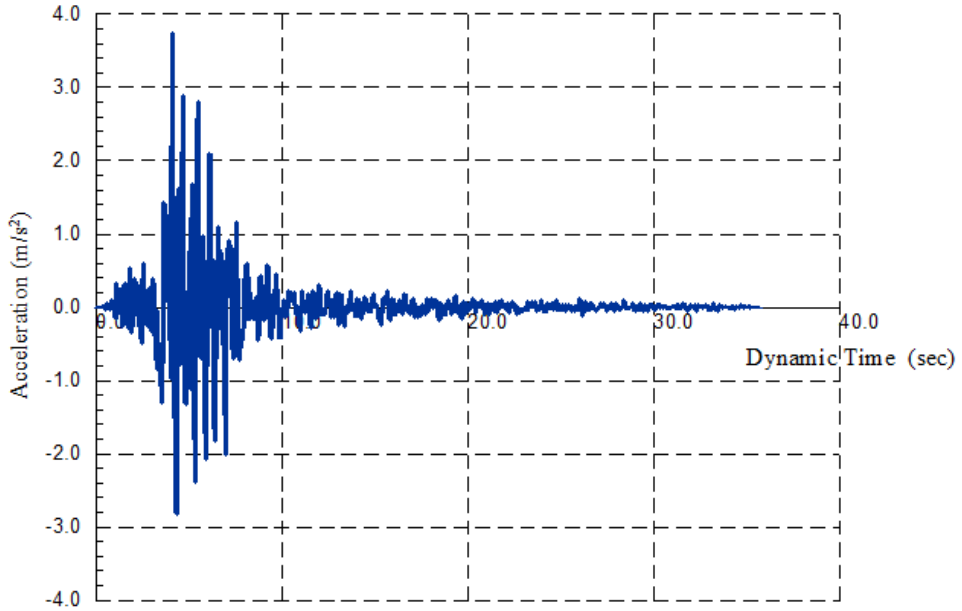


**Figure 12:** Friuli Earthquake Record.

Figures (13) presents comparison of displacement of a point at mud level between standard monopile with a diameter of 4.00 m and winged monopile with a diameter of 2.80 m affected by Northridge earthquake. Results show small variation between the standard and winged monopiles until the maximum earthquake displacement amplitude took place. After that, the standard monopile displacement are slightly lower than the top winged one mainly due to slight variation in the overall stiffness. The final dynamic displacements are slightly higher for the top winged monopile.

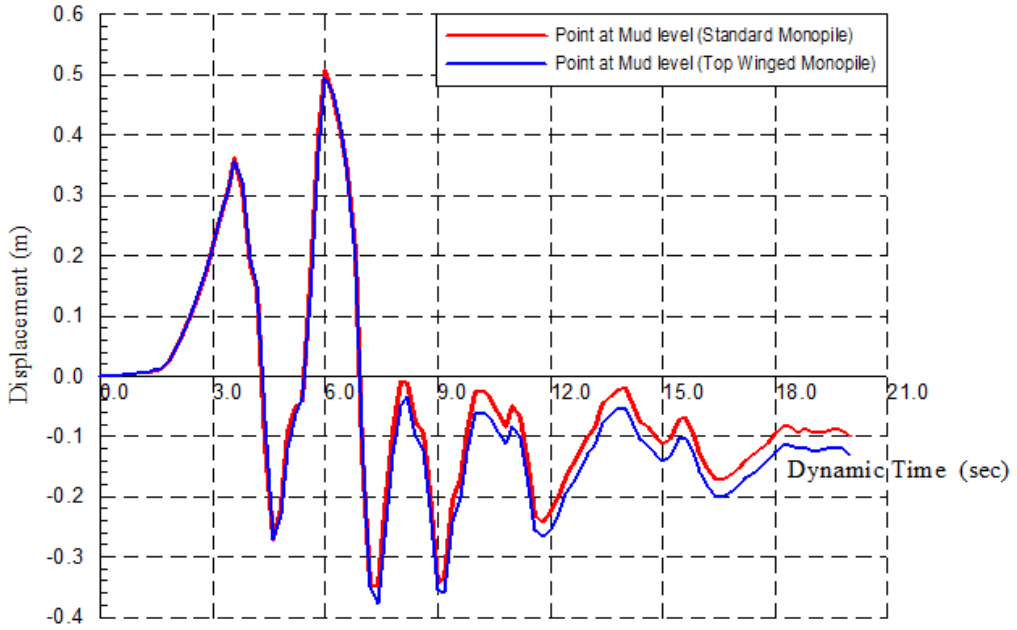


**Figure (13):** Comparison between Displacement-Time Histories of Standard Monopile and Top Winged One in Case of Northridge Earthquake Record.

Figure (14) reveals the displacement of a point at mud level caused by the Chi-Chi earthquake between a standard monopile with a diameter of 4.00 m and a winged monopile with a diameter of 2.80 m. During the earthquake, there is approximately no difference between standard and winged monopiles due to the lower number of displacement cycles in this record.

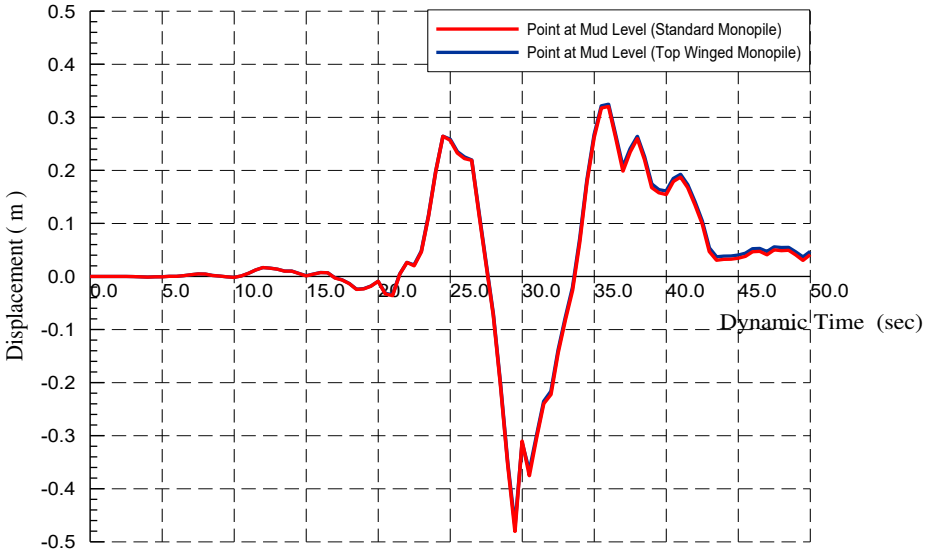


**Figure (14):** Comparison between Displacement-Time Histories of Standard Monopile and Top Winged One in Case of Chi-Chi Earthquake Record.

Figure (15) depicts the displacement of a point at mud level caused by the Friuli earthquake between a standard monopile and a top winged monopile. In the beginning slight differences are noticed between the behavior of the two monopiles. However, as the shaking of the monopiles began to increase, slight to moderate differences between the calculated mud level displacements became noticeable till the end of the dynamic record.

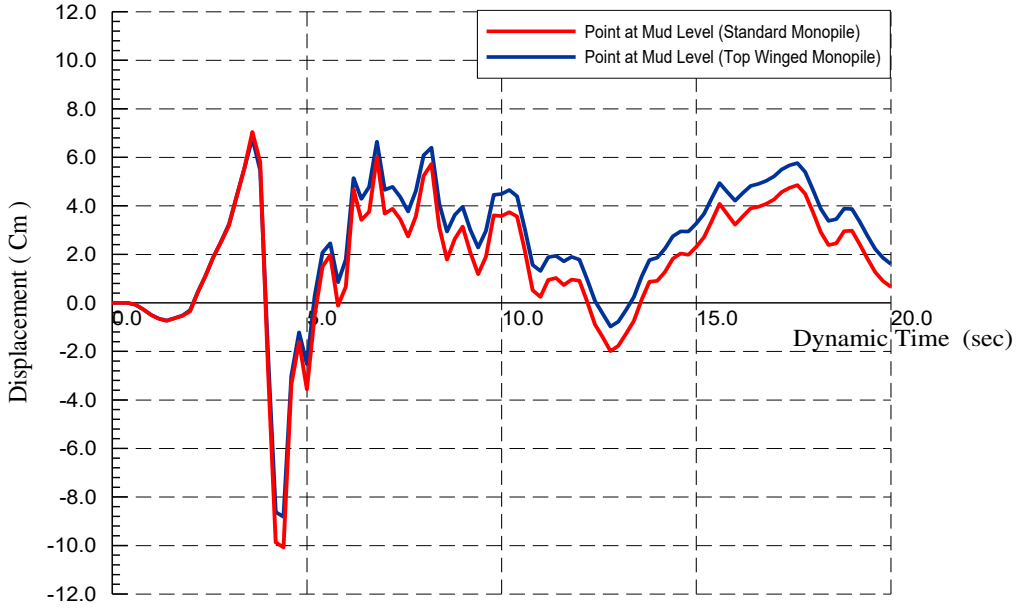


**Figure (15):** Comparison between Displacement-Time Histories of Standard Monopile and Top Winged One in Case of Friuli Earthquake Record.

### 4.3. Displacement-Time History at Different Points along the Monopile

Figure (16) illustrates the displacement-time history at the bed rock, the mud level, pile top, and pile tip during the Chi-Chi earthquake. The results show that the maximum displacement of all the studied points occurred at the same time as the peak of the earthquake. It was also found that the maximum displacements occurred at the pile top, with the displacement at the pile top being 14% and 33% greater than the displacements at the mud level and the pile tip, respectively. It is also noticed that there is no time lag between the computed displacements at the different points along the monopile length. Displacement amplification also took place with maximum took place at the pile top, and lower computed values at the mud level and the pile tip.

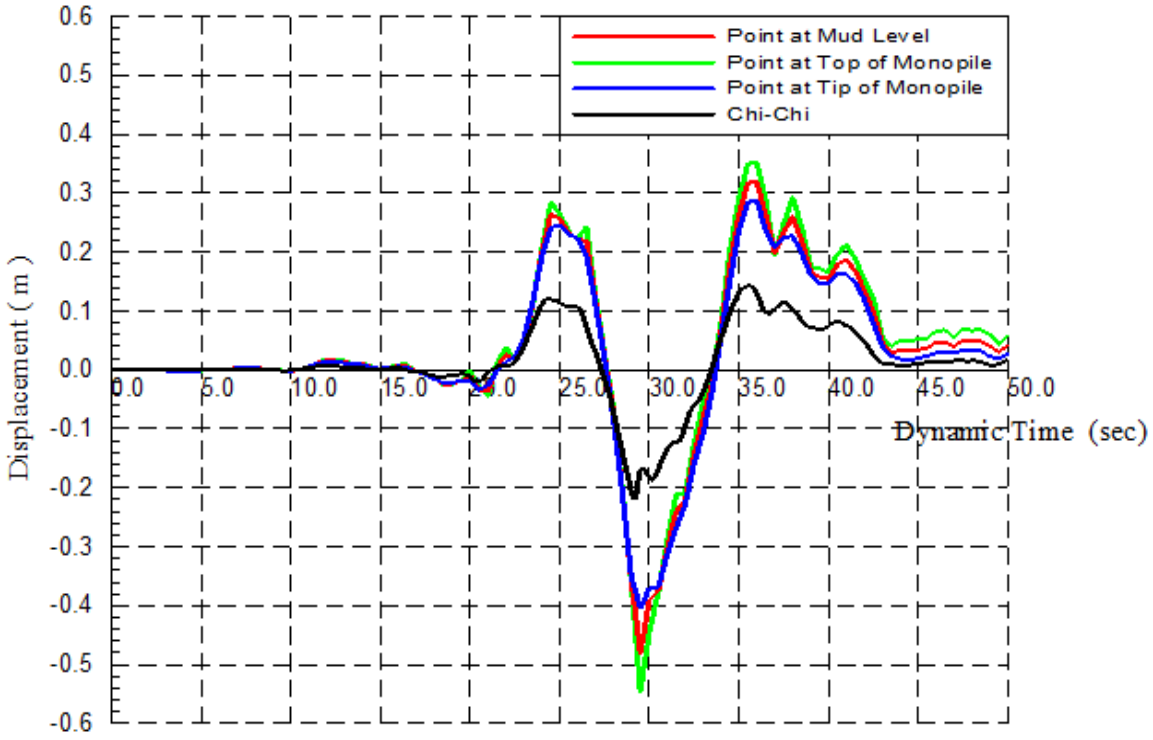


**Figure 16:** Displacement-Time History at Different Points along the Monopile for Chi-Chi case.

Figure (17) conveys the displacement-time history at the bed rock, mud level, pile top, and pile tip during the Friuli earthquake. The maximum displacement of all studied points took place at the same as the maximum displacement of the earthquake. It is also noted that the computed maximum displacement occurs at the pile top, with the displacement at the pile top being 52% and 150% greater than the displacement at the mud level and pile tip, respectively. Figure (17) also shows that the displacement amplifications are much larger under this earthquake record due to the relatively large number of variations in the earthquake record peaks.

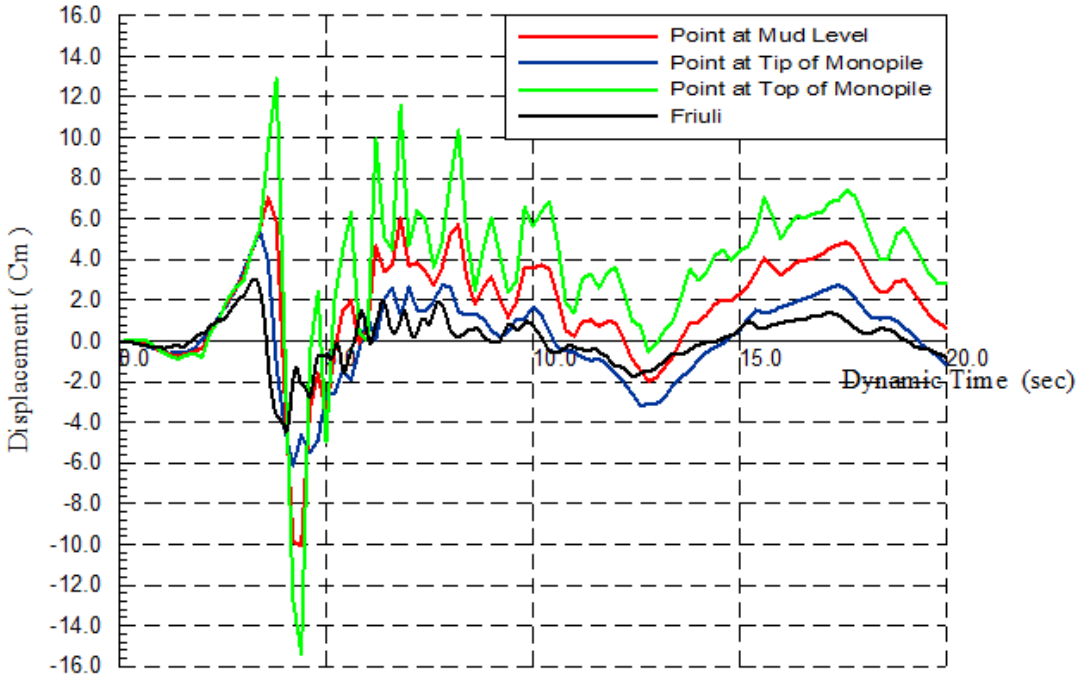


**Figure 17:** Displacement-Time History at Different Points along the Monopile for Friuli case.

## 5. CONCLUSIONS

1. The maximum displacement of all studied points along the pile length occurred at a time equal to the maximum earthquake displacement time. It is also noticed that the pile top has the maximum displacements.
2. The maximum positive excess pore water pressure occurred at the pile tip, but its value are much lower than the effective stresses and its duration is very small. Negative pore water pressures are also observed, mainly in the zone slightly below the pile tip.
3. Standard monopile with a diameter of 4.00 m has almost the same seismic behavior as using a winged monopile of a diameter of 2.80 m with additional wings which leads to lower material cost [15].
4. The difference between displacements in all cases caused by the plasticity and stiffness of the steel material of the wind turbine supporting structures and the non-linearity of the ground soil resistance and the frequency and signature of earthquake.
5. Displacement amplification also took place with maximum at the pile top, and lower computed values at the mud level and the pile tip.
6. Earthquake signature has a moderate effect in the seismic behavior of offshore monopiles.
7. Differences between the computed displacements of the standard and winged monopiles are much larger under earthquake records with relatively large number of variations in the earthquake record peaks.

## 6. REFERENCE

[1]- The European Wind Energy Association, (2015), "The European Offshore Wind Industry-Key Trends and Statistics", European Wind Energy Association: Brussels, Belgium.

[2]- DNVGL, (2016), "Support Structures for Wind Turbines", DNVGL Standard DNVGL-ST-0126; DNVGL: Oslo, Norway.

[3]- Det Norske Veritas, (2014), "Design of Offshore Wind Turbine Structures", Offshore standard DNV-OS-J101; Det Norske Veritas: Høvik, Norway.

[4]- Vanessa, S.; Hussam, and M. Multihazard, (2016), "Assessment of Wind Turbine Towers under Simultaneous Application of Wind, Operation, and Seismic Loads", J. Perform. Constr. Facil., 30, 04016043.

[5]- Katsanos, E.I.; Thöns, S.; Georgakis, C.T., (2016),"Wind Turbines and Seismic Hazard: A State-of-the-Art Review", Wind Energy, 19, p.2113-2133. [CrossRef]

[6]- Lavassas, I.; Nikolaidis, G.; Zervas, P.; Efthimiou, E.; Doudoumis, I.N.; and Baniotopoulos, C.C., (2003), "Analysis and Design of the Prototype of a Steel 1-MW Wind Turbine Tower", Eng. Struct., 25, p.1097-1106. [CrossRef]

[7]- Prowell, I., (2011), "An Experimental and Numerical Study of Wind Turbine Seismic Behavior", Ph.D. Thesis, University of California, Oakland, CA, USA.

[8]- Sapountzakis, E.J.; Dikaros, I.C.; Kampitsis, A.E.; and Koroneou, A.D., (2015), "Nonlinear Response of Wind Turbines under Wind and Seismic Excitations with Soil-Structure Interaction", J. Comput. Nonlin. Dyn., 10. [CrossRef]

[9]- Ma, H., (2012), "Seismic Analysis for Wind Turbines Including Soil-Structure Interaction Combining Vertical and Horizontal Earthquake", In Proceedings of the 15th World Conference on Earthquake Engineering, Lisbon, Portugal, p.24-28, September.

[10]- Kourkoulis, R.S.; Lekkakis, P.C.; Gelagoti, F.M.; and Kaynia, A.M., (2014), "Suction Caisson Foundations for Offshore Wind Turbines Subjected to Wave and Earthquake Loading: Effect of Soil-Foundation Interface", Géotechnique, 64, p.171-185. [CrossRef]

[11]- Anastasopoulos, I., and Theofilou, M., (2016), "Hybrid Foundation for Offshore Wind Turbines: Environmental and Seismic Loading", Soil Dyn. Earthq. Eng., 80, p.192-209.

[12]- Lysmer, J., and Kuhlemeyer, R.L., (1969), "Finite Dynamic Model for Infinite Media", ASCE, Journal of the Engineering Mechanics Division, 95, 4, p. 859-878.

[13]- Galavi, V., Petalas, A., and Brinkgreve, R., (2013), "Finite Element Modelling of Seismic Liquefaction in Soils", Geotechnical Engineering Journal of the SEAGS & AGSSEA, 44 (3).

[14]- Joyner, W.B. and Chen, A.T., (1975), "Calculation of Nonlinear Ground Response in Earthquakes", Bulletin of the Seismological Society of America, 65(5): p. 1315-1336.

[15]- Tarek N. Salem and Mohamed M. Hussein., (2021), “Laterally Loaded Monopile for Large Scale Offshore Wind Turbines", Tobacco Regulatory Science journal, 7(6–1): p. 6780-6796.

[16]- Mall, P. K., et al. "A comprehensive review of deep neural networks for medical image processing: Recent developments and future opportunities. Healthcare Analytics, 4, 100216." (2023).

[17]- Narayan, Vipul, et al. "Severity of Lumpy Disease detection based on Deep Learning Technique." 2023 International Conference on Disruptive Technologies (ICDT). IEEE, 2023.

[18]- Narayan, Vipul, et al. "A Comprehensive Review of Various Approach for Medical Image Segmentation and Disease Prediction." Wireless Personal Communications 132.3 (2023): 1819-1848.

[19]- Mall, Pawan Kumar, et al. "Rank Based Two Stage Semi-Supervised Deep Learning Model for X-Ray Images Classification: AN APPROACH TOWARD TAGGING UNLABELED MEDICAL DATASET." Journal of Scientific & Industrial Research (JSIR) 82.08 (2023): 818-830.

[20]- Saxena, Aditya, et al. "Comparative Analysis Of AI Regression And Classification Models For Predicting House Damages İn Nepal: Proposed Architectures And Techniques." Journal of Pharmaceutical Negative Results (2022): 6203-6215.

[21]- Kumar, Vaibhav, et al. "A Machine Learning Approach For Predicting Onset And Progression"“Towards Early Detection Of Chronic Diseases “." Journal of Pharmaceutical Negative Results (2022): 6195-6202.

[22]- Chaturvedi, Pooja, A. K. Daniel, and Vipul Narayan. "A Novel Heuristic for Maximizing Lifetime of Target Coverage in Wireless Sensor Networks." Advanced Wireless Communication and Sensor Networks. Chapman and Hall/CRC 227-242.

[23]- Kumar, Vaibhav, et al. "A Machine Learning Approach For Predicting Onset And Progression"“Towards Early Detection Of Chronic Diseases “." Journal of Pharmaceutical Negative Results (2022): 6195-6202.

[24]- Narayan, Vipul, et al. "7 Extracting business methodology: using artificial intelligence-based method." Semantic Intelligent Computing and Applications 16 (2023): 123.

[25]- Mall, Pawan Kumar, et al. "A comprehensive review of deep neural networks for medical image processing: Recent developments and future opportunities." Healthcare Analytics (2023): 100216.